

Volumetric motility-contrast imaging of tissue response to cytoskeletal anti-cancer drugs

Kwan Jeong¹, John J. Turek², David D. Nolte¹

¹Department of Physics, Purdue University, West Lafayette, Indiana 47907-2036

²Department of Basic Medical Sciences, Purdue University, West Lafayette, Indiana 47907

Corresponding author: nolte@physics.purdue.edu

Abstract: Microscopic imaging of cellular motility has recently advanced from two dimensions to three dimensions for applications in drug development. However, significant degradation in resolution occurs with increasing imaging depth, limiting access to motility information from deep inside the sample. Here, digital holographic optical coherence imaging is adapted to allow visualization of motility in tissue at depths inaccessible to conventional motility assay approaches. This method tracks the effect of cytoskeletal anti-cancer drugs on tissue inside its natural three-dimensional environment using time-course measurement of motility within tumor tissue.

©2007 Optical Society of America

OCIS codes: (090.1760) Computer holography; (110.6150) Speckle imaging; (170.1650) Coherence imaging; (170.3880) Medical and biological imaging.

References and links

1. R. D. Vale, "The molecular motor toolbox for intracellular transport," *Cell* **112**, 467-480 (2003), <http://download.cell.com/pdfs/0092-8674/PIIS0092867403001119.pdf>.
2. R. D. Vale and R. A. Milligan, "The way things move: Looking under the hood of molecular motor proteins," *Science* **288**, 88-95 (2000), <http://www.sciencemag.org/cgi/reprint/288/5463/88.pdf>.
3. E. Karsenti and I. Vernos, "The mitotic spindle: A self-made machine," *Science* **294**, 543-547 (2001), <http://www.sciencemag.org/cgi/reprint/294/5542/543.pdf>.
4. N. Hirokawa, "Kinesin and dynein superfamily proteins and the mechanism of organelle transport," *Science* **279**, 519-526 (1998), <http://www.sciencemag.org/cgi/reprint/279/5350/519.pdf>.
5. A. Desai and T. J. Mitchison, "Microtubule polymerization dynamics," *Annu. Rev. Cell Dev. Biol.* **13**, 83-117 (1997), <http://mitchison.med.harvard.edu/publications/AnnRevCelDevBioV13p83.pdf>.
6. J. R. Peterson and T. J. Mitchison, "Small molecules, big impact: A history of chemical inhibitors and the cytoskeleton," *Chem. Biol.* **9**, 1275-1285 (2002).
7. M. A. Jordan and L. Wilson, "Microtubules and actin filaments: dynamic targets for cancer chemotherapy," *Curr. Opin. Cell Biol.* **10**, 123-130 (1998).
8. T. D. Pollard and G. G. Borisy, "Cellular motility driven by assembly and disassembly of actin filaments," *Cell* **112**, 453-465 (2003).
9. E. Cukierman, R. Pankov, D. R. Stevens, and K. M. Yamada, "Taking cell-matrix adhesions to the third dimension," *Science* **294**, 1708-1712 (2001), <http://stke.sciencemag.org/cgi/reprint/sci.294/5547/1708.pdf>.
10. D. J. Webb and A. F. Horwitz, "New dimensions in cell migration," *Nat. Cell Biol.* **5**, 690-692 (2003), <http://www.nature.com/ncb/journal/v5/n8/pdf/ncb0803-690.pdf>.
11. W. E. Moerner and D. P. Fromm, "Methods of single-molecule fluorescence spectroscopy and microscopy," *Rev. Sci. Instrum.* **74**, 3597-3619 (2003), <http://unicorn.ps.uci.edu/243/papers/SingleMolecule.pdf>.
12. R. H. Webb, "Confocal optical microscopy," *Rep. Prog. Phys.* **59**, 427-471 (1996).
13. M. D. Cahalan, I. Parker, S. H. Wei, and M. J. Miller, "Two-photon tissue imaging: Seeing the immune system in a fresh light," *Nat. Rev. Immunol.* **2**, 872-880 (2002).
14. K. Konig, "Multiphoton microscopy in life sciences," *J. Microsc.* **200**, 83-104 (2000).
15. J. Sharpe, U. Ahlgren, P. Perry, B. Hill, A. Ross, J. Hecksher-Sorensen, R. Baldock, and D. Davidson, "Optical projection tomography as a tool for 3D microscopy and gene expression studies," *Science* **296**, 541-545 (2002), <http://www.sciencemag.org/cgi/reprint/296/5567/541.pdf>.
16. J. Huisken, J. Swoger, F. Del Bene, J. Wittbrodt, and E. H. Stelzer, "Optical sectioning deep inside live embryos by selective plane illumination microscopy," *Science* **305**, 1007-1009 (2004), <http://www.sciencemag.org/cgi/reprint/305/5686/1007.pdf>.

17. M. G. L. Gustafsson, "Nonlinear structured-illumination microscopy: Wide-field fluorescence imaging with theoretically unlimited resolution," *Proc. Natl. Acad. Sci. USA* **102**, 13081-13086 (2005), <http://www.pnas.org/cgi/reprint/102/37/13081.pdf>.
18. T. A. Klar, S. Jakobs, M. Dyba, A. Egner, and S. W. Hell, "Fluorescence microscopy with diffraction resolution barrier broken by stimulated emission," *Proc. Natl. Acad. Sci. USA* **97**, 8206-8210 (2000).
19. T. -C. Poon, T. Yatagai, and W. Jüptner, "Digital holography – coherent optics of the 21st century: introduction," *Appl. Opt.* **45**, 821-821 (2006), <http://www.opticsinfobase.org/abstract.cfm?URI=ao-45-5-821>.
20. U. Schnars and W. P. O Jüptner, "Direct recording and numerical reconstruction of holograms," *Meas. Sci. Technol.* **13**, R85-R101 (2002).
21. P. Massatsch, F. Charrière, E. Cuhe, P. Marquet, and C. D. Depeursinge, "Time-domain optical coherence tomography with digital holographic microscopy," *Appl. Opt.* **44**, 1806-1812 (2005), <http://www.opticsinfobase.org/abstract.cfm?URI=ao-44-10-1806>.
22. K. Jeong, J. J. Turek, and D. D. Nolte, "Fourier-domain digital holographic optical coherence imaging of living tissue," *Appl. Opt.* **46**, 4999-5008 (2007), <http://www.opticsinfobase.org/abstract.cfm?URI=ao-46-22-4999>.
23. J. G. Fujimoto, "Optical coherence tomography for ultrahigh resolution in vivo imaging," *Nat. Biotechnol.* **21**, 1361-1367 (2003), <http://www.nature.com/nbt/journal/v21/n11/pdf/nbt892.pdf>.
24. A. F. Fercher, W. Drexler, C. K. Hitzenberger, and T. Lasser, "Optical coherence tomography - principles and applications," *Rep. Prog. Phys.* **66**, 239-303 (2003), <http://ej.iop.org/links/rwYjAM6fK/QOFm5GMz3BGDkKzjav5vpA/r30204.pdf>.
25. P. Yu, M. Mustata, L. Peng, J. J. Turek, M. R. Melloch, P. M. French, and D. D. Nolte, "Holographic optical coherence imaging of rat osteogenic sarcoma tumor spheroids," *Appl. Opt.* **43**, 4862-4873 (2004), <http://www.opticsinfobase.org/abstract.cfm?URI=ao-43-25-4862>.

1. Introduction

Life is animated. Motion is the over-arching characteristic that distinguishes living from inanimate matter. The cellular machinery that drives motion consists of molecular motors [1,2] and molecular tracks [3-5]. The most active use of this machinery occurs during mitosis in which the entire cellular structure is reorganized prior to and during division. For this reason, drugs that inhibit the motors and their tracks are common anticancer agents, arresting the cell cycle by arresting motion [6,7]. Microscopic imaging of cellular motility and motility-related gene expression is well-established in two dimensions [8] for applications of drug development. But cells in contact with flat hard surfaces do not behave the same as cells embedded in the extracellular matrix [9,10], and recent work has raised the dimensionality of cellular motility imaging from 2D to 3D, including microscopies such as confocal fluorescence [11,12], two-photon [13,14], optical projection tomography (OPT) [15], and single-plane illumination projection (SPIM) [16]. Lateral resolution in these cases is diffraction-limited at the surface of the 3D matrix but degrade with depth. Although structured illumination [17] and stimulated emission [18] approaches can beat that limit under special circumstances, these too suffer significant degradation in resolution with increasing probe depth, limiting access to the motility information except near the surface of the tissue.

In this paper, we show that coherence-gated digital holography detects motility as deep as 10 optical thickness lengths inside tissue. This capability opens the opportunity to use motility as a contrast agent imaging at depths inaccessible to conventional motility assay approaches. Coherence-gated digital holography is an interferometric imaging approach that measures motility with displacement sensitivity below a fraction of a wavelength, over a macroscopic lateral field of view up to 1 mm. We found that motility at depth appears in real-time holograms as dynamic speckle. Furthermore, we define a motility metric based on the coefficient of intensity variance per pixel that becomes a novel imaging contrast agent. We demonstrate that the motility metric enables direct visualization of the effect of cytoskeletal anti-cancer drugs on tissue inside its natural three-dimensional environment, allowing time-course measurements of tissue and cellular response to drugs.

Digital optics was born from the union of improved CCD (charge-coupled device) sensors with advances in computer performance. Digital recording without film development increases acquisition speed and reduces cost. Acquired digital images are directly controlled

by computer in real time. One application of digital optics is digital holography [19]. In digital holography, the conventional holographic film is replaced with a CCD array, and digital holograms are reconstructed numerically. In previous approaches to digital holography, the Fresnel approximation [20,21] has been used for numerical reconstruction, where the CCD camera is located between the Fourier plane and the image plane in a Fresnel off-axis regime. We recently developed a digital holographic optical coherence imaging (DHOCI) technique [22] where the CCD is located at the Fourier plane and short-coherence light is used to select the depth within the target from which coherent information is acquired. It combines digital holography with coherence-domain imaging [23,24]. The chief advantages of DHOCI are fast numerical reconstruction, digital Fourier filtering capacity, and high sensitivity for diffuse targets.

The spatial dynamic range for digital holography is the ratio of the linear field-of-view (width of the full field) divided by the smallest resolvable average displacement within a single speckle. The smallest resolvable average displacement depends on the bit-level of the camera, the wavelength of the probe light, and the number of scatterers within an exciting mode volume. For our values, the minimum resolvable average displacement per speckle is about $\lambda/30$. The spatial dynamic range for a linear field of view of several millimeters is therefore about $10^5:1$. This number is about 100 times larger than for conventional microscopy-based motility assays on two-dimensional cell cultures. This is because it combines the sensitivity of interferometry (that can detect sub-nanometer displacements in the best cases) with conventional large-field-of-view imaging. It is important to note that our spatial resolution in direct imaging is only about 10 microns. The longitudinal sensitivity is achieved purely because of the coherent nature of the technique and the role played by each speckle as a micro-interferometer.

2. Experimental set-up

The DHOCI system is composed of a short-coherence light source and an imaging Mach-Zehnder interferometer, as shown in Fig. 1(a). Short-coherence light passes an initial beam splitter (BS) to produce a reference beam and an object beam. Lens (L) performs the Fourier transform of the backscattered object beam, and a digital hologram is captured by a CCD camera at the Fourier plane where the object beam interferes with the reference beam that passes through the delay stage in the reference arm. Longitudinal scanning is performed by translating the delay stage with a stepper motor. A mode-locked Ti:sapphire laser (100 fs pulse duration, 100 MHz repetition rate) is used as the short-coherence light source (center wavelength of 840 nm with a bandwidth of 17 nm). The typical power of the object beam for tissue is 5 mW with a diameter of 1 mm. A 12-bit CCD camera with one mega-pixel resolution is used with an exposure time of 10 msec.

A digital hologram captured at the Fourier plane requires only a 2-D fast Fourier transform for numerical reconstruction. An example of numerical reconstruction is shown in Fig. 1(b), which shows the zero-order-suppressed image of a high-reflectivity letter @ on diffuse white paper. The reconstructed image consists of three components: a zero-order image, a real image, and a conjugate image. The three components are spatially separated in the reconstructed image but overlap in the margins between each component. The zero-order image is the main background in DHOCI, and can be suppressed by subtracting a non-zero-path-matched digital hologram from the zero-path matched digital holograms. The real image is the same as the conjugate image except for its spatial location and the opposite sign in its complex-conjugated value. Therefore, we select only the real image area for the data analysis shown here. Selected instances of digital reconstructions of a USAF target, part of an onion, and a rat osteogenic sarcoma tumor spheroid are shown in Figs. 1(c)-1(e). The second element of group 7 in the USAF target and an individual cell of the onion were resolved. The lateral resolution is approximately 4 microns.

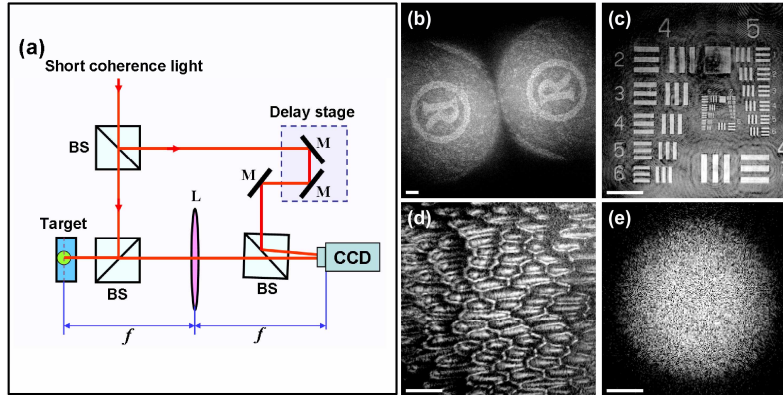


Fig. 1. (a) Schematic of the DHOCI system: M, Mirror; f , focal length. (b) Digital reconstruction of diffuse paper with letter Q. Selections of real images from digital reconstructions of (c) a positive UASF target, (d) inside onion at a depth of 100 μm , and (e) inside an 800- μm -diameter rat tumor spheroid at a depth of 400 μm , respectively. Bars, 200 μm .

3. Dynamic speckle and motility imaging

The reconstructed *en face* image of the rat tumor spheroid is striking in its absence of specific structure with its well-developed speckled quality. The rat osteogenic sarcoma tumor spheroids were grown *in vitro* in a rotating bioreactor. The spheroids may be grown up to several mm in diameter, and thus are large enough to simulate the thickness of different mammalian tissue. As tumor spheroids are cultured, they undergo cell apoptosis and necrosis in their center and so consist of an inner necrotic core with low activity and an outer shell with a thickness of 100- to 200- μm of viable proliferating cells with high motility. The speckle images of the tumor spheroids shimmer due to motility in tissue, and statistical properties of the dynamic speckle are obtained by capturing successive images at a fixed depth.

To capture dynamic speckle we acquired 40 successive digital holograms at a fixed depth and then reconstructed each to the image domain. The time interval between holograms is selected to be 1 second (in higher contrast mode) or 0.5 second (in higher speed mode). Examples of dynamic speckle are shown in Fig. 2 for the same rat tumor spheroid in two different conditions: healthy and chemically cross-linked. A “healthy” tumor is one that has been removed from the bioreactor and maintained in growth medium at room temperature for no more than 24 hours. For the cross-linked tumor, the proteins have been polymerized by the addition of 3% phosphate-buffered glutaraldehyde. Note the strong active motility of the healthy tumor (discontinuous vertical stripes) and the inactive motion of the cross-linked tumor (continuous vertical stripes) in the time-dependent cross-section data from the fixed-depth sections.

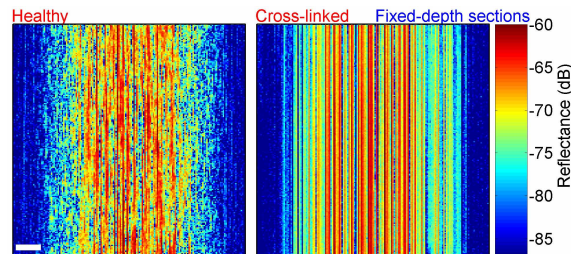


Fig. 2. Mid cross-section images from fixed-depth sections of a healthy tumor (left) and a cross-linked tumor (right). The data (acquired at a fixed depth of 340 μm from the top of a 680- μm -diameter tumor) are shown with a vertical axis of time. The healthy tumor shows significant fluctuations, while the cross-linked tumor is static. Bar, 100 μm .

The motility of the tissue in the viable shell and the necrotic core are quantified using a statistical approach. We developed a motility metric based on the normalized standard deviation (NSD) per pixel at fixed depth, which is the standard deviation divided by the average intensity. Large fluctuations in the dynamic speckle images result in high NSD value (and vice versa), and so a 2-D map of NSD values gives a visual measure of motility. An example of the motility imaging is shown in Fig. 3 for the healthy tumor. Average intensity maps are shown in the first column and standard deviation maps are shown in the second column, which were produced from 40 successive holographic images of a 900- μm -diameter tumor at a fixed depth of 430 μm from the tumor top. Motility maps (third column) were produced by 3-by-3 pixel averaging of normalized standard deviation (standard deviation divided by average intensity at each pixel). Average intensity maps and standard deviation maps are shown on a log scale. The object beam illuminated the center of the tumor for the first row and the edge of the tumor for the second row, which demonstrates that NSD value is in principle independent of illumination intensity. In the motility map, the dynamic area with high NSD values lies in a shell around the perimeter with a thickness of 100-200 μm , while the inactive area with low NSD values lies predominantly in the core. This matches the known morphology of the tumor spheroid with necrotic core and viable outer shell [25]. We averaged NSD values of the viable area (within about 150 μm thickness from the perimeter) and the necrotic area of healthy tumors with about 800 μm diameter (at a fixed depth of about 350 μm with time interval of 0.5 second between holograms). The NSD density ranged from 0.7 to 0.8 for the viable area and from 0.45 to 0.55 for the necrotic area of healthy tumors, averaging over about 30 tumors. This demonstrates that the viable area with strong motility can be distinguished from tissue with low activity through functional imaging in DHOCI using intrinsic motility as the only contrast agent.

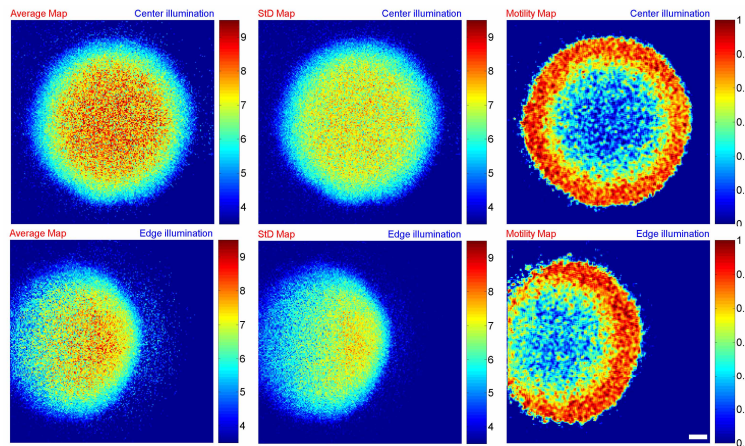


Fig. 3. An example of the motility imaging for a healthy tumor. Average intensity maps (first column), standard deviation maps (second column), and motility maps (third column) are shown for center illumination (first row) and edge illumination (second row) of the tumor. Motility images were produced under the same experimental conditions with a time interval of one minute, only by changing the position of the healthy tumor. The healthy tumor Bar, 100 μm .

Motility maps for the healthy tumor were generated at nine different depths (60, 120, 190, 260, 330, 390, 460, 530, and 600 μm from the tumor top), as shown in Fig. 4(a). In the motility maps, the region with low activity increases to the mid depth of the tumor and then decreases to the bottom of the tumor. The region of low activity is mainly centralized in the core of the tumor, correlating with active motility in the outer viable shell and with low or absent motility in the necrotic core. Motility maps for the cross-linked tumor are shown in Fig. 4(b). Motility maps for the cross-linked tumor show low NSD values for the entire volume at all depths because the cross-linked tumor has no activity. The average NSD value

for the cross-linked tumor is about 0.3, which is lower than the average NSD value for the necrotic volume of a healthy tumor. This difference is caused mainly by the shimmering shower-glass effect. In the healthy tumor, the necrotic volume is enveloped by the dynamic viable shell and so the light backscattered from the necrotic area shimmers by passing through the viable area, which causes an increase of the apparent NSD value for the necrotic area. However, the NSD value for the necrotic area is quantitatively lower than for the viable area, which indicates that the motility difference between dynamic tissue and inactive tissue can be detected, except with decreased contrast caused by the shimmering shower-glass effect.

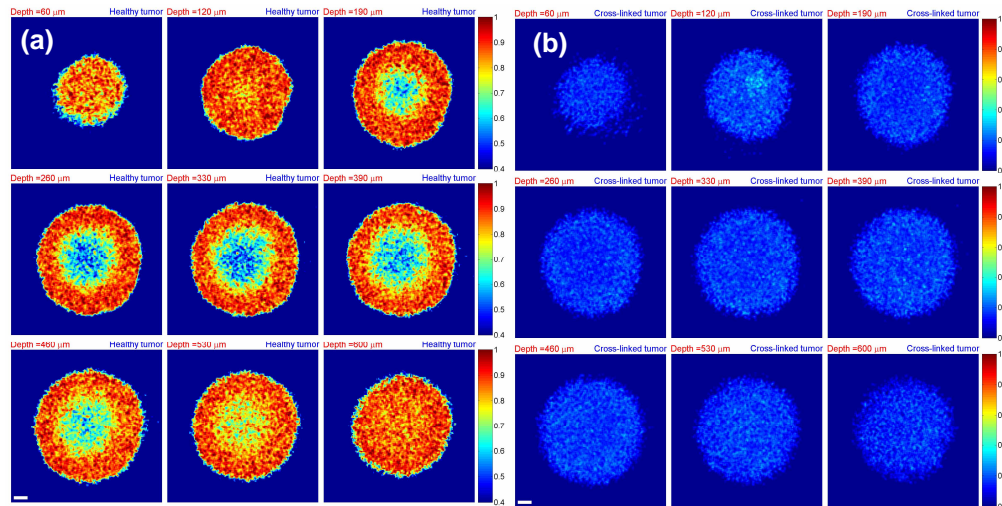


Fig. 4. Motility maps generated at nine different depths for (a) a healthy tumor and (b) a crosslinked tumor with a 680 μm diameter. Time interval between holograms was 1 second.

4. Tumor response to cytoskeletal drugs

We applied functional imaging to track the motility change in tissue in response to three cytoskeletal drugs: nocodazole, colchicine, and paclitaxel. Nocodazole and colchicine are anti-neoplastic drugs that disrupt microtubules by inhibiting polymerization of microtubules, and paclitaxel is an anti-neoplastic drug with the opposite effect that stabilizes microtubules by preventing depolymerization. Before tracking drug response in a tumor spheroid, motility maps for the healthy tumor were generated for 10 minutes with a 1 minute time interval to obtain the healthy base-line. After the treatment of the spheroid with drugs, time-course measurements to drug response were performed over three hours with 2-4 minute time intervals. An example of the time response to the drug nocodazole is given in Fig. 5 that shows motility maps as a function of time after treatment with 10 μg/ml nocodazole. In the motility maps, NSD values in the outer shell decrease with time, which correlates with the inhibition of microtubule dynamics in viable cells. Time-course motility maps in response to 10 μg/ml colchicine treatment showed a similar trend to those for 10 μg/ml nocodazole treatment, but with a slower drug response.

The time-course response of tissue to increasing concentrations establishes dose response curves. Graded concentrations of the cytoskeletal drugs nocodazole, colchicine and paclitaxel were added to the growth media of about 15 tumor spheroids. The motility response was measured at a fixed depth of about 350 μm (with tumor spheroids that ranged from 750 μm to 850 μm in diameter). The NSD density was obtained by the average of NSD values only in the viable area. Figures 6(a), 6(b), and 6(c) show varying response of the tumor spheroids to the drugs as a function of dose. The response of tissue to paclitaxel is small compared with other two drugs because paclitaxel stabilizes the microtubules. To obtain the dose response curves, the data were fit using single-exponential decay. Figure 6(d) shows the characteristic

reaction velocities in response to increasing dose of the three drugs, each fit to a first-order saturation curve. Nocodazole had an effective concentration for 50% response (EC_{50}) at 20 ng/ml compared to colchicine at 2 $\mu\text{g/ml}$ and to paclitaxel at 100 ng/ml, all within range of values obtained using two-dimensional cell cultures on other cell types. Nocodazole had a saturated reaction velocity three times larger than that of paclitaxel. These dose-response curves may be viewed as the characteristic “fingerprints” of the effect of each drug on motility.

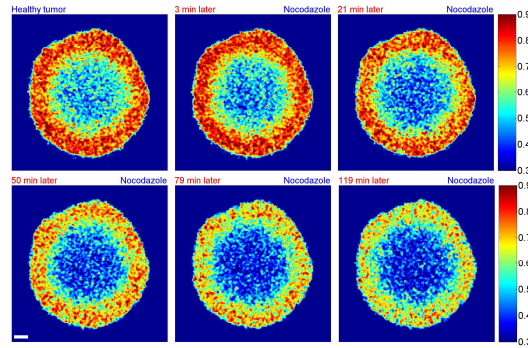


Fig. 5. Motility maps showing the response of an 820- μm -diameter tumor (at a fixed depth of 350 μm from the tumor top) to 10 $\mu\text{g/ml}$ nocodazole as a function of time (from healthy to 120 minutes later). Motility in the viable shell decreases with time, showing how nocodazole suppresses the activity of viable tumor cells. Bar, 100 μm .

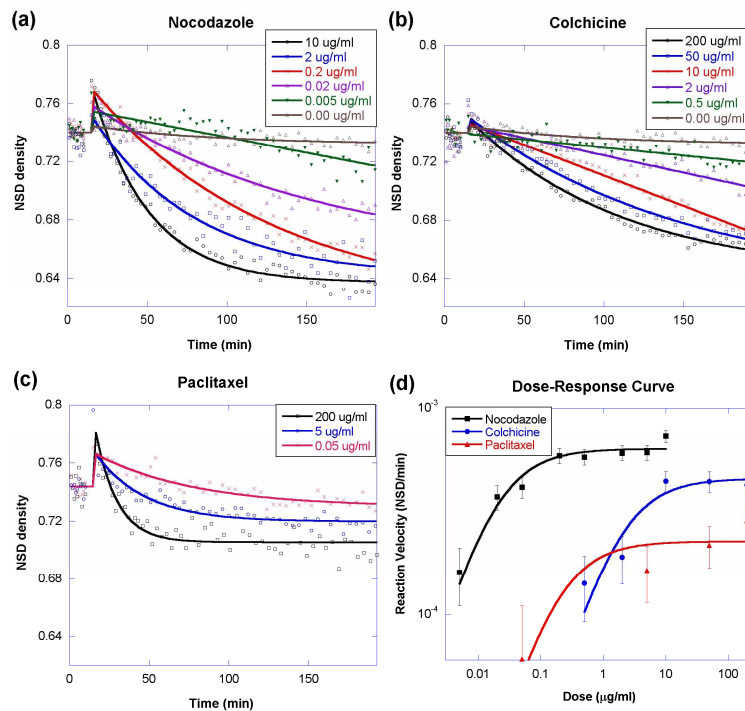


Fig. 6. Time-course measurements of NSD density (in the viable area) as a function of dose for (a) nocodazole, (b) colchicine, and (c) paclitaxel, respectively, showing dramatic motility decrease with increasing time and dose. (d) Reaction velocity (NSD/min) dose-response curves of three anti-neoplastic drugs, which are obtained from the characteristic time and magnitude of the time-response curves of NSD density in (a), (b), and (c).

5. Conclusion

The results presented here show the first demonstration of motility assays performed inside living tissue at depths inaccessible to conventional motility assay approaches. The deep tissue is far from any interfering surfaces that may alter the intercellular signalling. The technique has interferometric sensitivity to cellular displacements of a fraction of a wavelength by treating each speckle as an independent interferometer. The ability to measure sub-micron displacements over a field of view of a millimeter represents a large dynamic range that could prove useful for applications of high-throughput assays to monitor tissue response to drug candidates in drug development.

Acknowledgments

This work was supported by the National Science Foundation under grant BES-0401858.